Joint inversion of transient pressure and dc resistivity measurements acquired with in-situ permanent sensors: A numerical study

Faruk O. Alpak[1], Carlos Torres-Verdín[1], and Tarek M. Habashy[2]

ABSTRACT

We develop a quantitative methodology to interpret jointly in-situ transient pressure and dc resistivity measurements acquired in a hypothetical water injection experiment, with the goal of displacing oil in a hydrocarbon-bearing formation. The assumed measurement acquisition system consists of enforcing time-variable flow rates while injecting water into the surrounding rock formations, thereby producing a sequence of repeated transient pressure pulses. In-situ dc resistivity measurements are acquired at the end of every flow-rate pulsing sequence. The objective of the experiment is to estimate the spatial distributions of absolute fluid permeability and electrical resistivity. Geophysical inverse theory is used to account for the presence of noisy measurements.

Synthetic data with noise are inverted to assess the relative benefits of different types of sensor geometries in axisymmetric models of permeability and electrical resistivity. Results strongly suggest that cooperative inversion of in-situ transient pressure and dc resistivity measurements reduces nonuniqueness in the estimation of resistivity and absolute permeability governed by dynamic fluid-flow phenomena. This leads to a more accurate estimate of permeability and resistivity compared to separate inversion of each data type.

INTRODUCTION

The availability of permanently installed downhole pressure, resistivity, and temperature sensors has opened a new window of opportunity to probe hydrocarbon reservoirs. Permanent sensors and monitoring systems provide continuous streams of measurements that facilitate real-time reservoir management and therefore help to optimize hydrocarbon recovery. Several published papers describe the added value of perma-nent downhole pressure sensors when used as a part of a well completion, including Baker et al. (1995) and Athichanagorn et al. (1999). Data sets with enhanced resolution properties can be acquired with pressure sensors cemented behind casing and in direct hydraulic communication with rock formations. In-situ sensors of this type are placed in the annulus between the formation and the casing, remaining exposed to the hydraulics of formation fluids. Patents have been granted for cemented formation pressure sensors (Babour et al., 1995) and cemented resistivity arrays (Babour et al., 1997). Oilfield experiments have been conducted to test the practicality, feasibility, and added value of in-situ permanent sensors. Descriptions and results of such field tests are reported by van Kleef et al. (2001), Bryant et al. (2002a), and Bryant et al. (2002b), among others. These proof-of-concept field tests have created a renewed interest in dynamic monitoring and reactive management of complex hydrocarbon reservoirs. When linked to a feedback control mechanism such as remotely operated valves, interpretation of continuous streams of data provide an optimal management strategy for real-time control of fluid production/injection rates.

In contrast to sensor development and deployment issues, advances reported in the interpretation of data acquired with in-situ permanent sensors have been scarce. Athichanagorn et al. (1999) describe a wavelet analysis technique for the interpretation of permanent downhole pressure measurements and discuss practical issues related to processing large amounts of data. Belani et al. (2000) describe the utilization of permanent pressure sensors to monitor pressure transients with repeated fall-off tests. In the latter development, a method is described to interpret jointly cemented pressure- and resistivity-sensor data into estimates of saturation, front location, and fluid mobility ratios. Raghuraman and Ramakrishnan (2001) also combine in-situ permanent resistivity array measurements with cemented pressure-sensor data to constrain quantitatively fracture thickness, fracture absolute fluid permeability, and fracture porosity within an actual reservoir. Charara et al. (2002) perform a numerical experiment to demonstrate the use of

permanent resistivity and transient pressure measurements for time-lapse saturation monitoring. Wang and Horne (2000) integrate permanent resistivity sensor and production data to improve the estimation of spatial distributions of absolute fluid permeability.

The problem considered in this paper consists of mapping discrete time- and space-domain variations of in-situ transient pressure measurements as well as discrete space-domain measurements of dc resistivity voltages into spatial distributions of resistivity and absolute fluid permeability. To establish a proof of concept for the joint inversion algorithm developed in this paper, we use synthetic examples where measurements are generated numerically using accurate simulation algorithms. Numerical examples involve cases where synthetically generated measurements are contaminated with various degrees of random Gaussian noise. For practicality, we refer to absolute fluid permeability from this point onward as permeability.

In this paper, the inversion study is focused to the case of 2D axisymmetric spatial models of permeability and electrical resistivity. A cylindrical permeable medium with an injection well at its center is assumed as the reservoir geometry. We also assume that petrophysical layers describe the spatial heterogeneity of the formation of interest. The specific geometrical model considered in this paper is illustrated in Figure 1. A layer-by-layer spatial distribution of porosity is assumed available from well-log measurements such as density and/or neutron logs. On the other hand, fluid viscosity and compressibilities

Figure 1. Graphical description of a generic in-situ permanent-sensor installation along a vertical well. In-situ pressure sensors and point-contact dc electrodes are deployed in direct hydraulic communication with the formation. In this example, water is injected through an open well interval, thereby displacing in-situ oil. Water fronts in the form of cylinders with variable radii are used to indicate variability in the vertical distribution of permeability and electrical resistivity.

are assumed known from fluid sample analysis. In practical field applications, the parameters that we assume to be known may not be known at all or their values may involve various degrees of uncertainty, depending on the amount and spatial extent of measurements acquired within the particular formation of interest. Nonetheless, our assumptions involve measurable quantities and they become increasingly relevant with the quality and spatial extent of the measurements listed above.

We focus the analysis on two measurement strategies for in-situ transient pressure data. In the first strategy, transient pressure measurements are acquired during the shut-in period subsequent to a constant step injection rate pulse. In the second strategy, a more complete time record of pressure measurements is acquired during one injection and two fall-off periods of a multipulse cycle. In both cases, resistivity surveys are performed at the end of the transient pressure acquisition period. During fall-off periods, injection is stopped. The transient response of formation pressure generated by the change of injection rate (q_{inj} becomes zero) is recorded by in-situ sensors. During the subsequent injection period, the water injection process resumes. As such, a new pressure transient is generated from the injection rate pulse (when injection rate is increased from zero to q_{inj}). We also investigate the sensitivity of the inversion to the presence of random measurement noise.

IN-SITU PERMANENT SENSORS

Pressure sensors

In-situ permanent pressure sensors are cemented behind casing. Direct hydraulic communication between in-situ pressure sensors and surrounding rock formations is established via special perforation techniques that use shaped charges. Deployment practices of in-situ pressure sensors require novel well completion techniques to ensure the accurate placement and, hence, the reliable operation of these sensors. Techniques for the placement of in-situ permanent pressure sensors are the subject of active research and field test applications. Current practices described in the literature generally involve in-situ pressure sensors deployed across observation and production wells. Installation of in-situ pressure sensors across injection wells, on the other hand, represents a more challenging task because the isolation of the in-situ sensor from the wellbore hydraulics becomes increasingly less trivial. However, for hydrocarbon-bearing formations undergoing a waterflood operation, a soon-to-be-published numerical sensitivity study shows that in-situ transient pressure measurements acquired across injection wells have higher spatial sensitivity to the spatial distribution of permeability than the measurements acquired in a distant observation well. Therefore, in this paper we assume the availability of special completion designs and installation techniques that allow the deployment of in-situ permanent pressure sensors along the open-to-flow sections of injection wells.

Electrode arrays

The electrical tool considered in this work consists of an array of electrodes cemented in place within the annular space between electrically insulated casing and the formation. In the vertical direction, the array is deployed outside the electrically insulated part of the casing. A multiconductor cable serves as

the interface between each electrode and a surface switch connected to a power module. The basic acquisition consists of (1) establishing a dc current circuit between one of the electrodes and a surface grounding point and (2) measuring the potential induced on the remaining electrodes with respect to a surface reference electrode. This operation is repeated until all of the electrodes in the array have been used as dc current sources. The depth of investigation of the resistivity array is controlled by both the thickness of the rock formation straddled by the array and the resistivity contrast between the background rock formations and the injected fluid (van Kleef et al., 2001).

Unlike open-hole electrical logging devices, permanently deployed resistivity arrays offer the possibility of performing long-term and time-lapse measurements. Applications for permanent resistivity monitoring can be categorized into (a) waterflood front monitoring from either an observation or an injector/producer well, (b) water coning monitoring from a producer well, or (c) regional water table monitoring from an observation well or from the heel of a horizontal producing well (van Kleef et al., 2001).

PETROPHYSICAL MODEL

Our inversion approach is based on the cooperative use of electrical and fluid-flow measurements acquired in porous and permeable rocks. Injection of water into otherwise hydrocarbon-saturated rocks causes a variation of electrical resistivity as a result of the contrast in electrical resistivity between in-situ and injected fluids. When water is injected through the wellbore, the original distribution of resistivity becomes space dependent within the surrounding rock formation. In the presence of a homogeneous rock formation, the spatial distribution of fluid saturation resulting from injection becomes symmetric with respect to the axis of the borehole. Under some restrictive assumptions, the radial distribution of fluid saturation away from the injection well can be described approximately with sharp radial boundaries between coaxial, cylindrical blocks (Ramakrishnan and Kuchuk, 1993). We assume that fluid saturation within each block remains constant.

When density and viscosity of water and in-situ oil saturating the porous medium are close to each other, an approximate single-phase flow model can be formulated for simulating time- and space-domain distributions of formation pressure in the two-phase flow environment. In this formulation, one uses the dependence of effective permeabilities on end-point saturations and on end-point relative permeabilities. Note that the effective permeability k_{eff} of a porous medium for a given phase i is defined as the product of the absolute permeability k of the porous medium and the relative permeability k_r of the porous medium with respect to that phase, i.e., $k_{eff,i}(S_i) \equiv k k_{ri}(S_i)$. Then, relative and effective permeabilities of a porous medium for a given phase i depend on the saturation of that phase S_i.

We assume negligible capillary effects. We further assume that the densities and viscosities of the injected and in-situ fluids are close to each other. Thus, we can make the first-order assumption that the injected and in-situ fluids are separated by a sharp front. In this case, residual oil saturation prevails behind the injected-water front, where the water saturation is given by $S_w = S_{wor}(\equiv 1 - S_{or})$. Similarly, irreducible water saturation S_{wirr} prevails ahead of the advancing water front, where $S_w = S_{wirr}$. Therefore, the radial saturation pro-

file is represented by a jump discontinuity. In other words, instead of a relatively smoother Buckley-Leverett (Buckley and Leverett, 1942) saturation variation, we assume that sharp boundaries separate the leading and trailing saturation zones for each layer. Then, behind the injected water front, the effective permeability of the porous medium for the water phase equals $k_{eff,w} = k k_{rw}(S_{wor}) = k k_{rw}^o$, where k_{rw}^o is the end-point relative permeability for the water phase. Again, behind the injected water front, the effective permeability of the porous medium for the in-situ oil phase is $k_{eff,o} = k k_{ro}(S_{wor}) = 0$ because $k_{ro}(S_{wor}) = 0$. On the other hand, ahead of the advancing water front the effective permeability of the porous medium for the water phase $k_{eff,w}$ equals $k k_{rw}(S_{wirr}) = 0$ because $k_{rw}(S_{wirr}) = 0$. Yet the effective permeability of the porous medium for the oil phase is nonzero and is given by $k_{eff,o} = k k_{ro}(S_{wirr}) = k k_{ro}^o$, where k_{ro}^o is the end-point relative permeability for the oil phase.

We assume that during the time scale of transient pressure measurements, the location of the front remains stationary. This assumption is valid for injection rates that produce slow-moving fronts in waterflood operations. Consequently, the spatial distribution of effective permeabilities can be described by means of $k_{eff,w} \equiv k_I$ behind the water front and $k_{eff,o} \equiv k_{II}$ ahead of the front. As such, for the approximate single-phase flow model, which assumes a slowly moving front within the measurement time scale of pressure transients, the layer-by-layer distribution of effective permeabilities can be described by means of a model that consists of a two-zone equivalent absolute fluid permeability per layer. For the fluid-flow domain, the parameters k_I, k_{II}, and r, where r is the distance of the injected water front from the center of the injection well, remain as the primary variables governing the physics of transient-pressure measurements.

The above approach renders the simulation of in-situ pressures equivalent to a problem of single-phase flow of a slightly compressible fluid (water + oil) in an inhomogeneous permeable medium. Having made the above assumption, the governing partial differential equation of the flow problem in a 2D axisymmetric geometry is solved by using a robust and efficient method described in the previous section. We also assume a negligible salinity gradient between injected and in-situ irreducible water. Consequently, for a water injection application in an axisymmetric single-well geometry, the above-described equivalent permeability segments per horizontal layer naturally coincide with the coaxial-cylindrical resistivity blocks used to describe the spatial distribution of fluid saturation. This observation emphasizes the fact that the near-borehole petrophysical model is consistent in both electrical resistivity and fluid-flow domains.

We approximate the effects of fluid saturation variability within each horizontal layer (due to two-phase flow) using lumped elements described in terms of behind- and ahead-of-the-front equivalent permeabilities and resistivities. Permeabilities and resistivities behind and ahead of the front are spatially constrained by means of the location of the injected water front. In our petrophysical model, the (end-point) saturations that describe the radial saturation variability are utilized implicitly within the equivalent permeability concept. As such, no assumption is required about the specific values of these saturations. Spatial heterogeneity in the vertical direction is assumed in the form of horizontal flow units (or layers) intersecting

the coaxial-cylindrical blocks that describe the fluid saturation distribution. Figure 2 is a graphical description of the parametric model assumed in this paper to describe the spatial distributions of permeability and electrical resistivity between the injection well and the observation well, and between the observation well and the outer boundary of the reservoir.

From a measurement viewpoint, the properties of the spatial distributions of resistivity can be estimated with dc electrical measurements (i.e., voltages). On the other hand, the spatial distribution of permeability governs the in-situ transient pressure response of rock formations surrounding the injection well. Although spatial variations of electrical resistivity and permeability can cause uncoupled perturbations of in-situ transient pressure and electric voltage measurements, an indirect coupling exists between the description of the physics of fluid-flow phenomena and the physics of dc electrical phenomena. In effect, the parameter r that defines the radial location of each petrophysical block is common to the description and numerical simulation of the two types of measurements. We assume that additional petrophysical information about the segmentation blocks, i.e., the thickness and porosity of each flow unit, is readily available from other types of ancillary borehole measurements (e.g., density and gamma-ray logs). In general, information about the above-listed parameters involves various degrees of uncertainty. Quantitative interpretation of the borehole measurements for these parameters, and of their probabilistic integration into the fluid-flow model, represent tasks that remain outside the scope of this paper.

Within a given horizontal layer, we consider two coaxial cylindrical blocks (Figure 2). Accordingly, the inner radial boundary of the first cylindrical block is equal to the wellbore radius, whereas the outer radial boundary of the second cylindrical block is equal to the distance between the injection and production wells. The common radial boundary between the two cylindrical blocks is identified as r_i, where the subscript i designates the specific horizontal layer under consideration. Thereafter, we jointly invert the two types of measurements to yield values of electrical resistivity and permeability within each petrophysical block as well as the radial boundary location between the two coaxial cylindrical blocks.

The joint inversion approach, formulated for the petrophysical model described above, constrains the outcome of the inversion to honor measurements in both resistivity and fluid-flow domains. Subsequent to the joint inversion, using the inverted resistivity distribution, average fluid saturations behind and ahead of the front can be readily estimated by
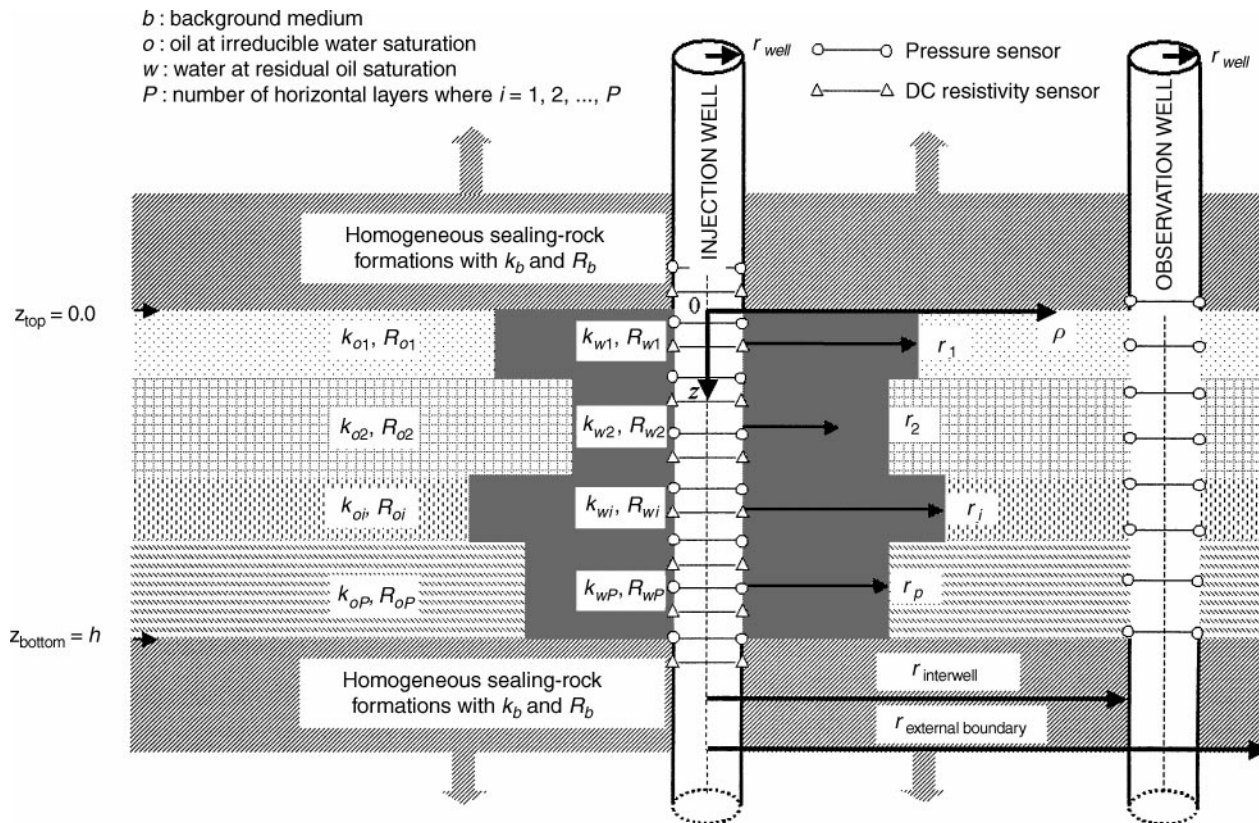
Figure 2. Graphical description of the parametric petrophysical model adopted for the joint inversions of in-situ measurements of pressure and dc resistivity. The petrophysical model is axial symmetric with respect to the axis of the injection well. Pressure and dc resistivity sensors are deployed along the injection well, while only pressure sensors are deployed along the observation well. The parametric description of the petrophysical model consists of a fixed number of horizontal layers. There are two concentric cylindrical blocks within each horizontal layer. The first cylindrical block has an inner radius equal to the borehole radius and a variable outer radius. The second cylindrical block has an outer radius equal to the distance between the injection well and the outer boundary of the reservoir and an inner radius equal to the outer radius of the first cylindrical block. Permeability and electric resistivity are assumed constant within a given cylindrical block.

enforcing an appropriate saturation equation, i.e., Archie's law (Archie, 1942), which honors the underlying physics of resistivity-saturation coupling.

The motivation in developing a joint inversion approach for transient pressure and dc resistivity measurements is to estimate petrophysical models that are consistent with the two types of measurements. As shown below, such a strategy provides an efficient way to reduce nonuniqueness in the inversions otherwise performed independently with the two sets of measurements.

NUMERICAL TECHNIQUES USED FOR MODELING AND INVERSION OF IN-SITU PERMANENT SENSOR MESUREMENTS

Quantitative studies have been performed to assess the value of transient in-situ permanent pressure-sensor measurements in detecting permeability variations in the proximity of a sensor deployment (Alpak et al., 2001). In this paper, components of the petrophysical model under investigation consist of permeability and electrical resistivity. We assume that the unknown petrophysical model can be parameterized with a finite and discrete number of variables. The corresponding inverse problem is solved by minimizing a quadratic cost function written as the sum of the square differences between the measured data and the data yielded by a forward modeling algorithm. A nonlinear Gauss-Newton fixed-point iteration search is used to minimize the quadratic cost function. This minimization strategy requires the computation of the Jacobian (sensitivity) matrix, whose entries consist of first-order variations of the cost function. Construction of the Jacobian matrix is the most computationally demanding component of the nonlinear inversion algorithm. Extensive research work in geophysical inverse theory has been undertaken to approximate, eliminate, and economize the computation of the Jacobian matrix. Torres-Verdín and Habashy (1994) and Ellis et al. (1993) describe alternative approaches for the effective computation of the Jacobian matrix. The inversion algorithm developed in this paper is based on an efficient least-squares minimization technique adapted from the work of Torres-Verdín et al. (2000). We also use a novel dual-grid approach to accelerate the inversion.

The dual-grid inversion algorithm relies on the iterative forward modeling of transient pressure and dc resistivity measurements. Accurate and computationally efficient forward modeling algorithms are used to simulate the measurements within the context of the inversion framework. These forward modeling algorithms are also used to generate synthetic measurements subsequently inverted in our numerical proof-of-concept studies. Simulations are consistently performed on numerical grids finer than the block scale parameterization assumed for the petrophysical model.

Numerical simulation of in-situ permanent sensor measurements

For modeling subsurface fluid flow, we assume that the density and viscosity of the injected water and of the in-situ oil phases are approximately equal to each other to justify the notion of a slightly compressible single-phase fluid-flow regime. Here, the compressibility used to describe the thermodynamic nature of the single-phase fluid is considered a volumetric average of the compressibilities of the injected water and in-situ oil

phases. As such, we consider the single-phase flow of a Newtonian fluid in a rigid porous medium occupying a bounded domain $\Omega \in R^3$ with a smooth boundary $\partial\Omega$. The conservation of mass over a representative control volume leads to the continuity equation (Muskat, 1937)

$$-\nabla \cdot [\rho(\mathbf{r}, t)\mathbf{v}(\mathbf{r}, t)] = \phi(\mathbf{r})\frac{\partial \rho(\mathbf{r}, t)}{\partial t}, \quad (1)$$

where ρ is the mass density, $\mathbf{v}$ is the velocity vector, ϕ is the time-invariant porosity distribution, $\mathbf{r}$ is a point in 3D space, and t is time. According to Darcy's law, the fluid velocity can be written as

$$\mathbf{v}(\mathbf{r}, t) = -\frac{\mathbf{K}}{\mu} \cdot \nabla p(\mathbf{r}, t), \quad (2)$$

where p is pressure, μ is fluid viscosity, and $\mathbf{K}$ is the second-order permeability tensor. We further assume the existence of a principal coordinate system in which the permeability tensor takes the simple diagonal form

$$\mathbf{K} = \begin{pmatrix} k_x & 0 & 0 \\ 0 & k_y & 0 \\ 0 & 0 & k_z \end{pmatrix}. \quad (3)$$

Finally, for a slightly compressible fluid with constant compressibility C_t and viscosity μ, the pressure-diffusion equation 1 can be written as

$$\nabla \cdot \left[\frac{\mathbf{K}}{\mu} \cdot \nabla p(\mathbf{r}, t)\right] = \phi(\mathbf{r})C_t\frac{\partial p(\mathbf{r}, t)}{\partial t}. \quad (4)$$

We solve equation 4 to numerically simulate time-domain measurements acquired with the in-situ pressure sensors for specific flow rate (time) schedules of water injection. In this paper, we use an algorithm that solves the governing partial differential equation on a 2D axisymmetric finite-difference spatial grid. The original diffusivity equation is converted into an equivalent finite-difference operator problem that is solved with an extended Krylov subspace method (EKSM) (Alpak, Torres-Verdín, Sepehrnoori et al., 2003). This single-phase flow forward modeling algorithm is implemented into a simulation code also called EKSM. The EKSM formulation yields multiple-time pressure computations with almost the same computer efficiency as that of a single-time simulation.

Numerical simulation of dc electrical responses

The differential equation satisfied by the electric potential $u(\mathbf{r})$ is given by

$$\nabla \cdot [\sigma(\mathbf{r})\nabla u(\mathbf{r})] = \nabla \cdot \mathbf{J}_S(\mathbf{r}), \quad (5)$$

where $\mathbf{r}$ is the observation point, $\sigma(\mathbf{r})$ is the distribution of electrical conductivity, and $\mathbf{J}_S(\mathbf{r})$ is the impressed dc current source. For the case in which a point electric current of strength I is enforced at $\mathbf{r}_S$ then $\nabla \cdot \mathbf{J}_S(\mathbf{r}) = -I\delta(\mathbf{r} - \mathbf{r}_S)$ and equation 5 simplifies to

$$\nabla \cdot [\sigma(\mathbf{r})\nabla u(\mathbf{r})] = -I\delta(\mathbf{r} - \mathbf{r}_S). \quad (6)$$

In this paper, a solution of equation (6) is approached with a numerical simulation algorithm based on the semidiscrete numerical approach that combines the method of straight lines with an incomplete Galerkin formulation scheme described

by Druskin and Knizhnerman (1987). This forward modeling algorithm is also implemented by the latter authors into a simulation code called NKARD. Within the joint inversion framework described in this paper, we make use of both NKARD and EKSM.

Minimized cost function

For the estimation of the 2D axisymmetric spatial distribution of petrophysical parameters of interest, permeability and electrical resistivity are assigned a constant value within each petrophysical block. Let $\mathbf{m}$ be the size N vector of unknown parameters that fully describe the axisymmetric distribution of petrophysical parameters and $\mathbf{m}_R$ be a reference vector of the same size as $\mathbf{m}$ that has been determined from some a priori information. We undertake the estimation (inversion) of $\mathbf{m}$ from the measured data by minimizing a quadratic cost function $C(\mathbf{m})$ defined as (Torres-Verdín and Habashy, 1994)

$$2C(\mathbf{m}) = \left[\left\| \mathbf{W}_d \cdot [\mathbf{d}(\mathbf{m}) - \mathbf{d}^{obs}] \right\|^2 - \chi^2 \right] + \lambda \|\mathbf{W}_m \cdot (\mathbf{m} - \mathbf{m}_R)\|^2, \qquad (7)$$

where $\mathbf{d}^{obs}$ is a size M vector that contains the noisy measured data and $\mathbf{W}_d \cdot \mathbf{W}_d^T$ is the inverse of the data covariance matrix. This data-weighing matrix describes the estimated variance for each particular measurement and the estimated correlation between measurements. The parameter χ denotes the prescribed value of enforced data misfit. A priori estimates of the noise in the measurements are employed to determine the magnitude of χ. In equation 7, $\mathbf{d}(\mathbf{m})$ is the measurement vector numerically simulated for specific values of $\mathbf{m}$; $\mathbf{W}_m \cdot \mathbf{W}_w^T$ is the inverse of the model covariance matrix, used to enforce a quantitative degree of confidence in the reference model $\mathbf{m}_R$ and to enforce a priori information on $\mathbf{m}$; and λ is a Lagrange multiplier or regularization parameter.

The first additive term on the right-hand side of equation 7 drives the inversion toward fitting the measurements within the desired χ value. The sole presence of such a term in the cost function $C(\mathbf{m})$ will yield multivalued solutions of the inverse problem as a result of both noisy measurements as well as insufficient and imperfect data sampling. Enforcing an extremely small data misfit may result in petrophysical models with exceedingly large model norms (Torres-Verdín and Habashy, 1994). The second additive term on the right-hand side of equation 1 is used to reduce nonuniqueness and to stabilize the inversion in the presence of noisy and sparse measurements. In this context, the Lagrange multiplier λ controls the relative weight of the two additive terms in the cost function. The developments considered in this paper use an efficient strategy to compute the regularization parameter described in Torres-Verdín and Habashy (1994). We implemented a search for the Lagrange multiplier such that a data misfit reduction of ξ, where $0.5 \leq \xi \leq 1.0$, was imposed at each iteration with respect to the data misfit achieved at the previous iteration. The search for an optimal Lagrange multiplier demanded typically five to ten evaluations of data misfit at each iteration. Such evaluations did not compromise the efficiency of the inversion primarily because of the fast forward modeling algorithms EKSM and NKARD and partly because of the dual-grid algorithm used to minimize the quadratic cost function.

Measurement and model vectors

In the above cost function, the measurement vector $\mathbf{d}^{obs}$ is constructed from discrete real values of dc resistivity data gathered in the form of electric potentials (voltage differences) u and/or space–time samples of pressure p in the following organized fashion:

$$\mathbf{d}^{obs} = \left[d_1^{obs}, d_2^{obs}, \ldots, d_M^{obs} \right]^T = [\mathbf{u}, \mathbf{p}]^T, \qquad (8)$$

where $\mathbf{u} = [u_1, u_2, \ldots, u_k]$ and $\mathbf{p} = [p_1, p_2, \cdots, p_L]$. In equation 8, M is the total number of measurements and the superscript T indicates transpose. The types of entries to be included in the measurement vector depend on the inversion approach. For an independent inversion, only either discrete pressure or electric potential values are included in the measurement vector. Each value of d^{obs} represents a measurement taken at a particular sensor location, current source depth (for resistivity surveys), or time (for transient pressure data). An inversion performed with a single measurement type is intended to yield only estimates of its associated petrophysical parameters. The joint inversion approach uses both types of measurements and is intended to produce (a) estimates of resistivity and permeability for each petrophysical block and (b) the location of the oil–water interface for each layer.

Similarly, the model vector can be assembled as

$$\boldsymbol{\eta} = [R_1, R_2, \ldots, R_\alpha; r_1, r_2, \ldots, r_\beta; k_1, k_2, \ldots, k_\gamma]^T, \quad (9)$$

where R_i and k_i denote block resistivity and permeability, respectively. The parameter r specifies the location of the oil–water interface; therefore, there is one r for each layer. In equation 9, the subscripts α, β, and γ are the number of resistivities, block-boundary locations, and permeabilities, respectively, that constitute the model subject to inversion. Then, the total number of model parameters N equals $\alpha + \beta + \gamma$. By denoting the model parameters as η_i, where $i = 1, 2, \ldots, N$, one has

$$\boldsymbol{\eta} = [\eta_1, \eta_2, \ldots, \eta_N]^T. \qquad (10)$$

A model vector constructed with only the model parameters R and $r = r_R$ is used for the independent inversion of electrical voltages. Likewise, an independent inversion of in-situ transient pressure measurements will involve only the model parameters k and $r = r_k$. For both joint and independent inversion approaches, an arbitrary combination of individual model parameters can be estimated, depending on the extent of information available a priori for the unknown model.

Given that all of the model parameters involved in the inversion are real and positive, we implement the change of variable $m_i = \ln(\eta_i)$, where $i = 1, 2, \ldots, N$. This change of variable is consistent with the fact that both electrical resistivity and permeability often exhibit a large range of variability. The vector of transformed model parameters is denoted by $\mathbf{m}$.

Gauss-Newton fixed-point iteration search

To determine a stationary point $\mathbf{m}$ where the cost function attains a minimum, we use a Gauss-Newton fixed-point iteration search (Gill et al., 1981). This method considers only first-order variations of the cost function in the neighborhood of a local iteration point. The corresponding iterated formula

can be written as

$$\mathbf{m}^{k+1} = \left[\mathbf{J}^T(\mathbf{m}^k) \cdot \mathbf{W}_d^T \cdot \mathbf{W}_d \cdot \mathbf{J}(\mathbf{m}^k) + \lambda \mathbf{W}_m^T \cdot \mathbf{W}_m \right]^{-1}$$
$$\cdot \left\{ \mathbf{J}^T(\mathbf{m}^k) \cdot \mathbf{W}_d^T \cdot \mathbf{W}_d \cdot [\mathbf{d}(\mathbf{m}^k) - \mathbf{d}^{obs} + \mathbf{J}(\mathbf{m}^k) \cdot \mathbf{m}^k] \right.$$
$$\left. + \lambda \mathbf{W}_m^T \cdot \mathbf{W}_m \cdot \mathbf{m}_R \right\}, \tag{11}$$

subject to

$$l_i \le m_i^{k+1} \le u_i, \quad \text{where} \quad i = 1, 2, \dots, N. \tag{12}$$

In the above expressions, the superscript k is used as an iteration count and $J(\mathbf{m})$ is the Jacobian matrix of $C(\mathbf{m})$. Upper and lower bounds enforced on $\mathbf{m}^{k+l}$ are intended to have the iterated solution yield only physically consistent results. The fixed-point iteration search for a minimum of $C(\mathbf{m})$ is concluded when the measured data have been fit within the prescribed tolerance, χ.

The inversion algorithm used in this paper also takes advantage of a novel cascade optimization technique that incorporates a dual finite-difference gridding approach to accelerate the inversion associated with a large number of unknown model parameters. This highly efficient least-squares minimization technique is adapted from the work of Torres-Verdín et al. (2000).

SENSITIVITY STUDIES FOR THE JOINT INVERSION OF PERMANENT SENSOR MEASUREMENTS

The foregoing nonlinear inversion algorithm is applied to the estimation of petrophysical model parameters, namely, permeabilities and electrical resistivities assuming a 2D axisymmetric geometry. A central objective of this work is to advance a proof of concept for the cooperative use of in-situ transient pressure and dc resistivity measurements. Attention is focused on a hypothetical test case in which water is injected from a vertical well into the surrounding oil-saturated rock formations to displace movable oil. Permanent in-situ pressure sensors are assumed to be positioned along the well's water injection interval as well as along a vertical observation well located some distance away from the injection well. We also assume that the resistivity array is deployed only along the injection well.

Six-block test case

The actual petrophysical model (Figure 3a) shows a vertical cross-section of the axisymmetric spatial distributions of permeability, layer-by-layer porosity, and resistivity around a vertical injection well. The spatial distribution of porosity is assumed to be known from ancillary measurements such as seismic and well-log data. A vertical observation well is located 72.2 m away from the injection well. Both the injection and the observation wells are equipped with 15 in-situ permanent pressure sensors, 11 of which are installed across the formation of interest and are evenly distributed along the corresponding well. In addition, two sensor couples are deployed at the top and bottom of the reservoir within the sealing impermeable layers.

We assume a resistivity array consisting of 18 uniformly distributed point-contact electrodes deployed along the injection well. Reservoir and fluid-flow parameters associated with this
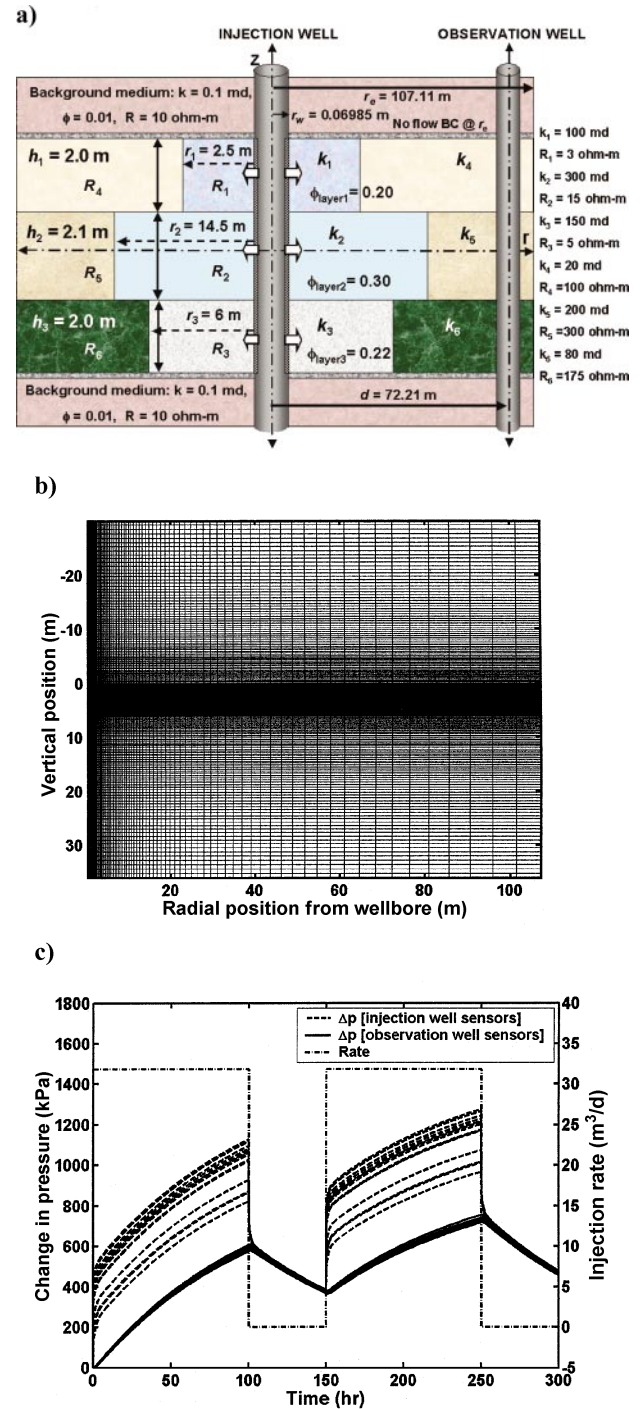
Figure 3. Six-block formation model. (a) Description of the permeable medium. The associated reservoir and fluid properties are listed in Table 1. Injection flow rates are modeled with a truncated-line source equivalent to a fully penetrated well. Both injection and observation wells are equipped with in-situ permanent pressure sensors. The resistivity array, consisting of dc point-contact electrodes, is deployed only along the injection well. (b) A finite-difference grid of size 134×249 in the r and z directions, respectively, is used for the forward and inverse modeling of in-situ transient-pressure measurements. (c) Superimposed plots of pressure change and flow rate as a function of time. The flow rate history consists of a periodic schedule of a 100-hr-long injection pulse followed by a 50-hr-long fall-off period.

inversion exercise are listed in Table 1. Data input to the inversion were simulated numerically using the EKSM and NKARD forward modeling codes.

A finite-difference grid measuring 134×249 in the radial and vertical directions, respectively, was constructed to perform the numerical simulations and inversions of in-situ transient pressure measurements. This grid, shown in Figure 3b, consists of logarithmic steps in the radial direction and a combination of logarithmic and linear steps in the vertical direction. Figure 3c displays a plot of the simulated time-varying pressure responses, Δp versus t, for all of the sensors deployed along the injection and observation wells. The associated time record of flow-rate measurements, q versus t, is superimposed to the plot of simulated transient pressures. Because of hydraulic communication among reservoir blocks, the sensitivity of in-situ transient pressure measurements to time variations of injection flow rate is relatively smaller along the observation well than along the injection well, as shown in Figure 3c.

For the simulation of the dc electrical measurements, a 201-node, logarithmically distributed radial mesh was entered into NKARD. The spatial distribution of nodes for this grid is shown in Figure 4a. Upper and lower reservoir boundaries are displayed together with the radial nodes. Figure 4b shows the electric potential measurements simulated along the electrode array as a function of both sensor number and depth. Single-time electric voltages measured at the end of the water injection schedule constitute the electrical data input to the inversion algorithm.

Table 1. Petrophysical and fluid-flow parameters used to construct the synthetic reservoir models.

Parameter	Value
Fluid viscosity, μ (Pa · s)	0.001
Total compressibility, C_t (kPa^{-1})	2.90×10^{-6}
Wellbore radius, r_w (m)	0.06895
Reservoir external radius, r_e (m)	107.11
Reservoir thickness, h (m)	6.10
Injection rate, q (step-function pulse), (m^3/d)	31.80

We first investigate the joint and independent inversions of in-situ transient pressure measurements acquired during a fall-off period (subsequent to a constant step injection-rate pulse) and electrical measurements acquired during a resistivity survey at a time corresponding to the end of the pressure fall-off period. More specifically, transient pressure measurements acquired during the first fall-off period of the multipulse cycle (Figure 3c), are considered as input data to the inversion. In this acquisition strategy, transient pressure measurements are recorded during the time interval between the 100th and the 150th hour of the flow rate pulse schedule. In the case of joint inversion, transient pressure measurements are inverted in conjunction with electrical measurements. Alternatively, a more complete time record of measurements acquired during one injection and two fall-off periods of the multipulse cycle is inverted both independently and in conjunction with electrical measurements. For these two latter cases, we considered transient pressure measurements acquired during the first fall-off, second injection, and second fall-off periods of the multipulse cycle displayed in Figure 3c as input. Henceforth, we refer to the latter measurement set as multipulse and to the former type of measurement set as single-pulse in-situ transient pressure measurements.

We perform both independent and joint inversions of the spatial distribution of permeability and resistivity. For the independent inversions, only in-situ transient measurements are used when estimating permeability, and only electric potential measurements are used when estimating resistivity. Next, we conduct joint inversions of the spatial distribution of permeability and resistivity. Figure 5 shows vertical cross-sections (radial distance versus vertical location) of the actual and inverted spatial distributions of permeability obtained using both independent and joint inversion approaches. Inversion results obtained with the use of single- and multipulse transient pressure responses for both inversion approaches are also shown in Figure 5. The spatial locations of in-situ pressure sensors deployed along the injection and observation wells are displayed on the same cross-section plots. Analogous sets of plots for the spatial distributions of electrical resistivity are shown in
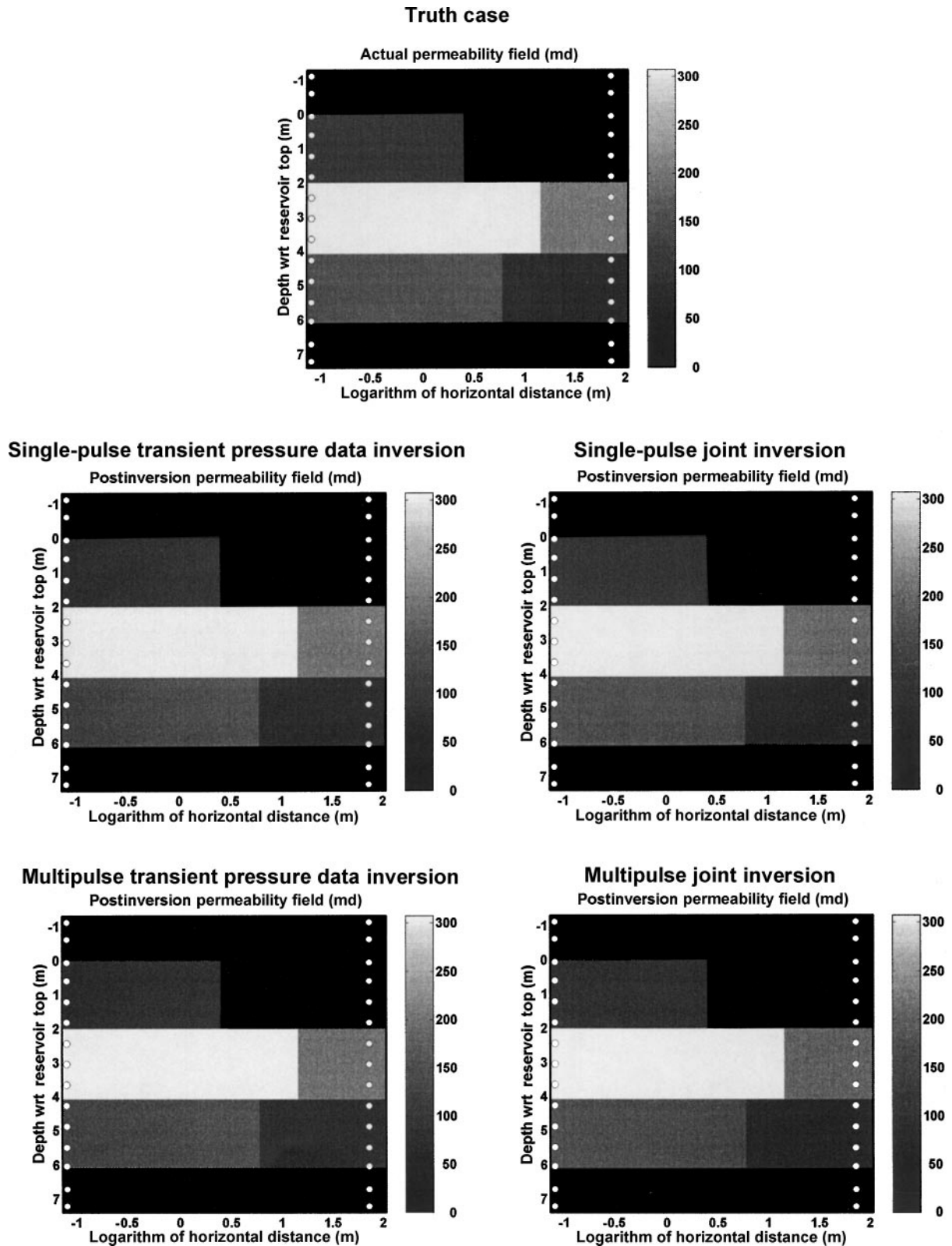
a)

b)

Figure 4. (a) Finite-difference radial grid constructed with 201 logarithmically distributed nodes. This mesh is used for the forward and inverse modeling of dc resistivity measurements. The forward modeling algorithm only requires the use of a radial grid. (b) The dc electrical response: voltage measurements acquired with point-contact electrodes deployed along the injection well.

Truth case

Actual permeability field (md)

Single-pulse transient pressure data inversion

Postinversion permeability field (md)

Single-pulse joint inversion

Postinversion permeability field (md)

Multipulse transient pressure data inversion

Postinversion permeability field (md)

Multipulse joint inversion

Postinversion permeability field (md)

Figure 5. Six-block formation example, with actual and postinversion spatial distributions of permeability. Parametric estimations are performed with independent inversions of noise-free single- and multipulse in-situ transient pressure measurements and, alternatively, with joint inversions of noise-free single- and multipulse in-situ transient pressure and dc resistivity measurements. Locations of in-situ pressure sensors in the injection and observation wells are indicated with small circles. The term *wrt* = with respect to.

Figure 6. The spatial location of the 18-electrode dc resistivity array is superimposed to the cross-section of resistivity shown in Figure 6. For the estimation of model parameters k (permeability) and r (radial boundary location), the mean value of each individual parameter was used as the initial guess for the inversions. However, for electrical resistivity R, the initial guess was constructed from the mean value of each vertical set of segments. Experiments performed with other initial-guess locations indicated that the inversion algorithm did not yield estimations biased by the change of the initial guess. In all cases, inversion results converged to the global minimum, rendering postinversion model-domain errors smaller than 1%.

Although model-domain percent errors were relatively small for this exercise, results obtained with the joint inversion approach consistently yielded smaller model-domain percent errors than those yielded by independent inversions. For instance, for the independent inversion of the spatial distribution of permeability using multipulse in-situ transient pressure measurements, the maximum model domain error was 0.294%, whereas for an equivalent joint permeability–resistivity inver-

sion, the maximum model-domain error decreased to 0.102%. Comparison of inversion results attained with the use of single- and multipulse in-situ transient pressure measurements did not indicate a significant advantage of one approach over the other for those cases that assumed noise-free measurements. Relative data misfits computed with the formula

$$\frac{\left\| \mathbf{W}_d \cdot [\mathbf{d}(\mathbf{m}^k) - \mathbf{d}^{obs}] \right\|^2}{\left\| \mathbf{W}_d \cdot \mathbf{d}^{obs} \right\|^2} \tag{13}$$

yielded misfit values smaller than 1.0×10^{-4} for all of the noise-free inversions considered in this section. In-situ transient-pressure data-domain fits for the injection and observation well are shown in Figures 7a and 7b, respectively. In addition, Figure 7c displays postinversion data-domain fits for the measured dc resistivity voltages. Excellent data fits were common for inversions performed with noise-free measurements. Numerical experiments also showed that the regularization term in equation 11 was not necessary for the stability and
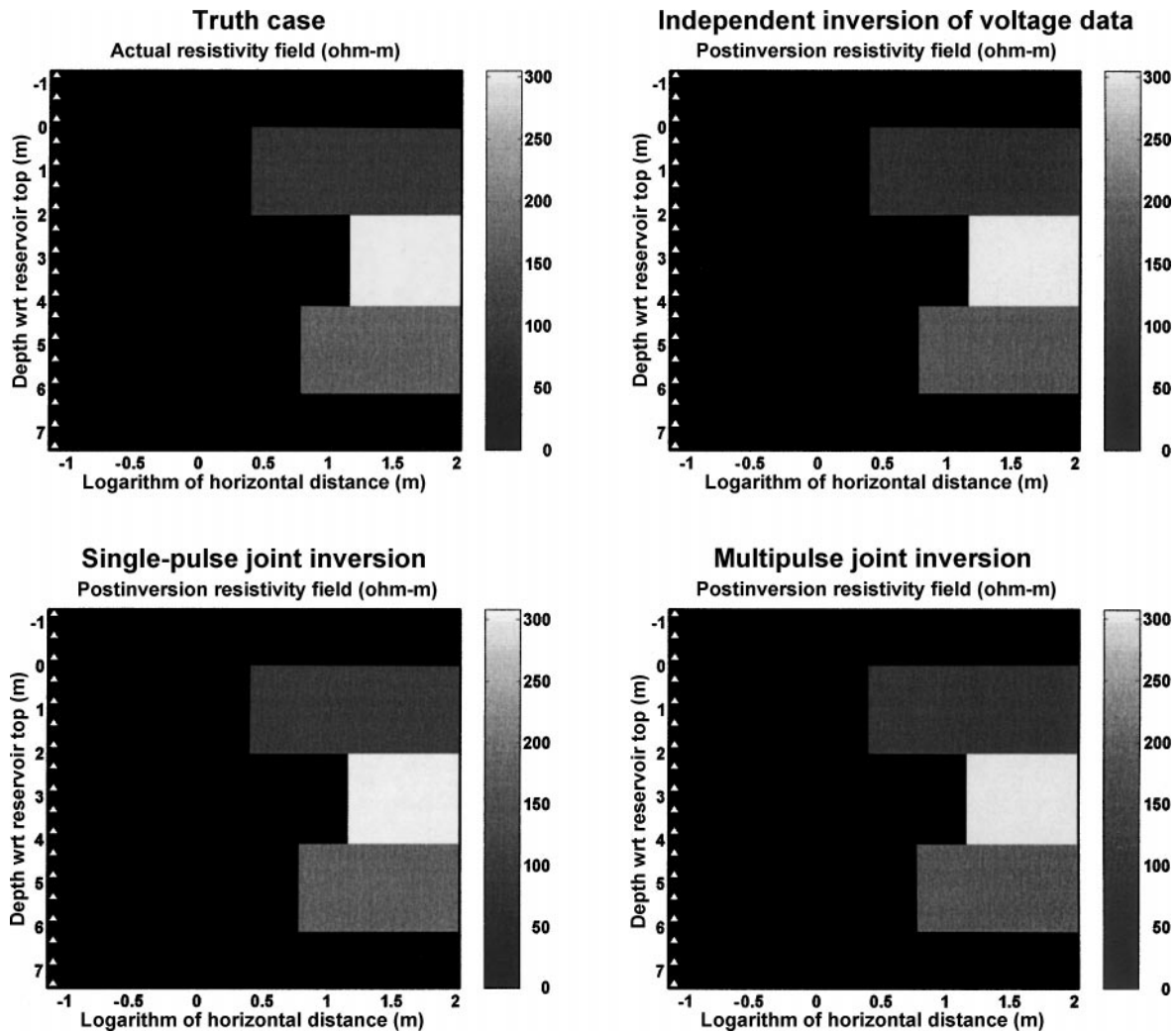
Figure 6. Six-block formation example, with actual and postinversion spatial distributions of resistivity. The estimated spatial distributions are obtained from independent inversions of noise-free dc resistivity measurements and, alternatively, from joint inversions of noise-free single- and multipulse in-situ transient pressure and dc resistivity measurements. Locations of in-situ contact electrodes (resistivity sensors) in the injection well are indicated with small triangles. The term *wrt* = with respect to.

convergence of the inversion algorithm when noise-free measurements were used.

A study was also performed to assess the influence of noisy measurements on the inverted six-block model parameters. We first considered a test example wherein single- and multipulse transient pressure measurements were contaminated with 1% zero-mean random Gaussian noise. Independent inversions of transient pressure measurements were performed to assess the impact of noise. Postinversion reconstructions of the permeability domain are shown in Figure 8 for both single- and multipulse transient pressure measurements along with the actual permeability distribution. Percent error maps for the quantitative estimation of permeability values in each parametric block are also shown for the investigated cases. Note that these er-
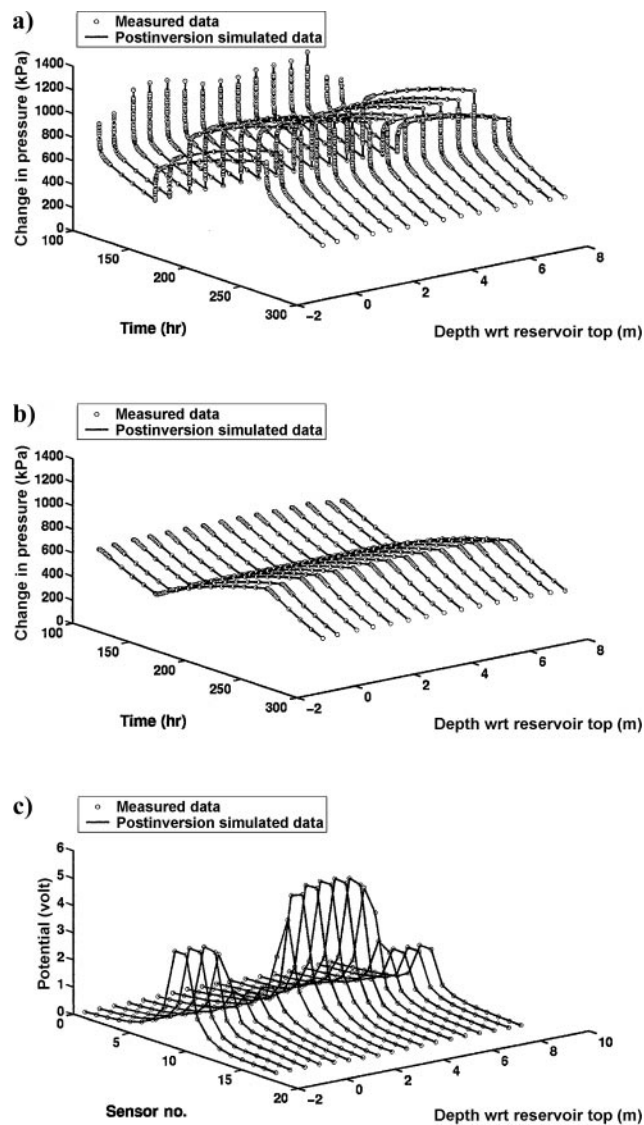
Figure 7. Six-block formation example. Plots of measured and postinversion simulated in-situ transient pressures along the (a) injection and (b) observation wells. (c) Plots describing measured and postinversion dc resistivity voltages along the injection well. Inversion of the spatial distribution of permeability and resistivity was performed jointly from noise-free multipulse in-situ transient pressure and dc resistivity measurements. The term *wrt* = with respect to.

ror maps do not quantify the error in the reconstruction of block-boundary locations (parameter r). Inversion results indicate accurate reconstructions of the near-borehole permeability distribution in the vicinity of the injection well. However, inversion results for the permeability blocks away from the injection well are negatively influenced by the deleterious effect of noise.

A similar test example was considered wherein dc resistivity measurements were contaminated with 1% zero-mean random Gaussian noise. We first investigated the independent inversion of dc resistivity measurements. Postinversion reconstructions of the resistivity domain are shown in Figure 9 along with the actual resistivity distribution. A percent error map for the quantitative estimation of resistivity values in each parametric block is also shown in Figure 9. Note that this error map does not quantify the error in the reconstruction of block-boundary locations (parameter r). Similar to the independent inversion of noisy transient pressure measurements, inversion results indicate accurate reconstructions of the model parameter (in this case, resistivity) distribution in the vicinity of the injection well. Yet inversion results for the resistivity blocks away from the injection well are negatively influenced by the deleterious effect of noise.

To provide a quantitative proof of concept for the merit of the joint inversion algorithm, we first consider the test example wherein both the simulated in-situ multipulse transient pressure and dc voltage measurements are contaminated with 1% zero-mean additive random noise simulated with a Gaussian pseudorandom number generator. Noisy in-situ transient pressure and dc resistivity (voltage) measurements are then inverted jointly to yield the coupled spatial distributions of permeability and resistivity. Inversion results indicate accurate reconstructions of the spatial distributions of permeability and resistivity. Subsequently, joint inversion of transient pressure and dc resistivity measurements was repeated for the case where the noise level in the measurements was increased to 2%.

Figure 10 compares the spatial distributions of permeability and resistivity inverted from noisy measurements with the actual spatial distributions of these parameters. A comparison of the spatial distributions of permeability and resistivity inverted from noisy and noise-free measurements is also shown in this plot. The noisy case shown in Figure 10 is the one where measurements were contaminated with 2% Gaussian random noise. Inversion results obtained with noisy measurements suggest a robust estimation of petrophysical parameters under the deleterious influence of measurement noise. For both permeability and resistivity, model parameters near the injection well were estimated more accurately than the model parameters for petrophysical blocks located farther away from the injection well. Even though the frames showing the spatial distribution of resistivity in Figures 9 and 10 are not shown with the same scale, the true distribution of resistivity does remain the same for the two cases described by these figures. Results from the independent inversion approach, shown in Figure 9, yielded relatively larger errors in the spatial distribution of resistivity. Therefore, we opted to describe the results graphically using an extended resistivity scale that included all of the resistivity values yielded by the independent inversion. Despite the increased level of measurement noise used in the joint inversion, the estimated resistivities exhibited a small degree of variability. Accordingly, Figure 10 was constructed using a narrower resistivity range than in Figure 9.
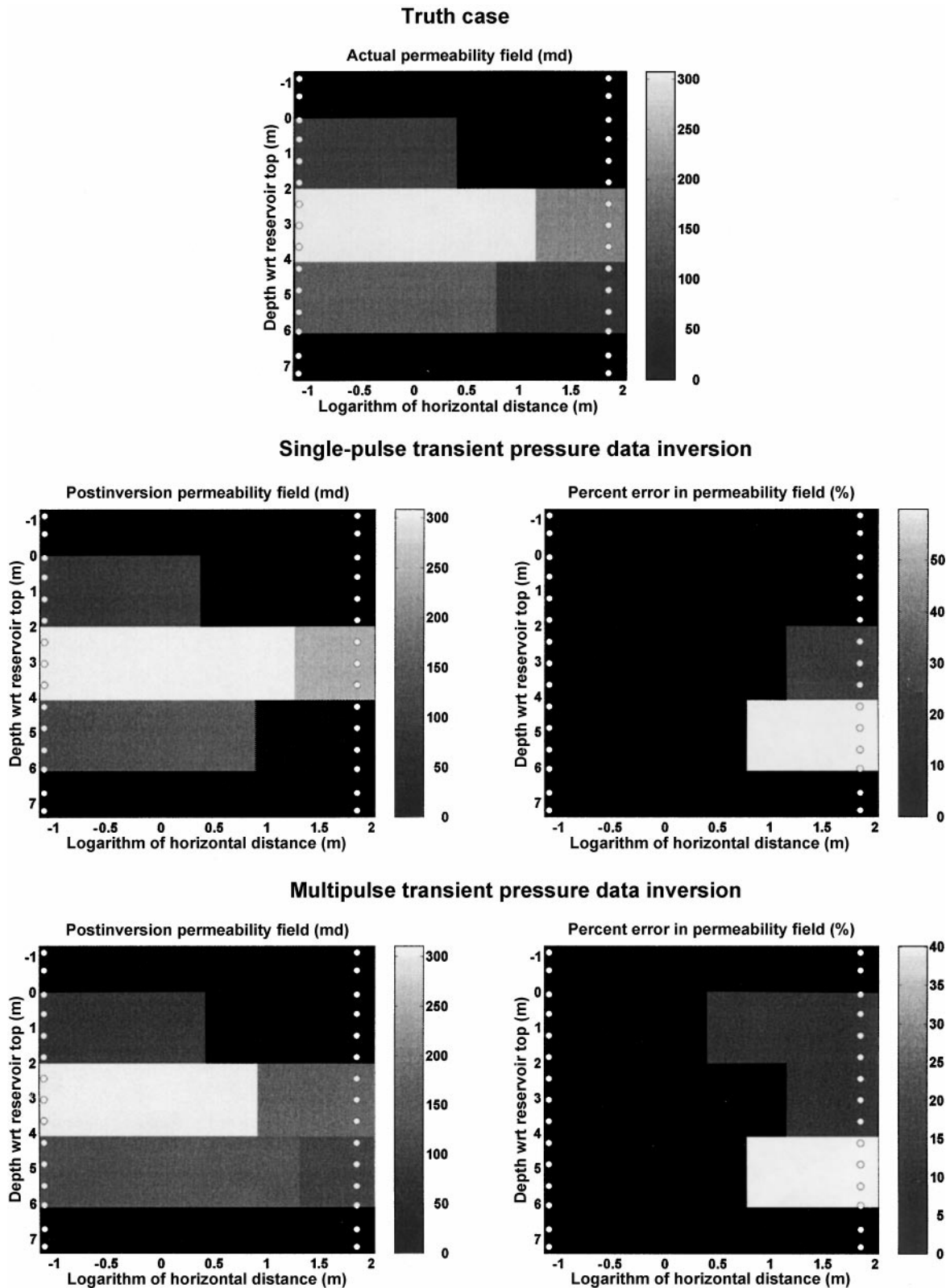
Truth case

Actual permeability field (md)

Single-pulse transient pressure data inversion

Postinversion permeability field (md)

Percent error in permeability field (%)

Multipulse transient pressure data inversion

Postinversion permeability field (md)

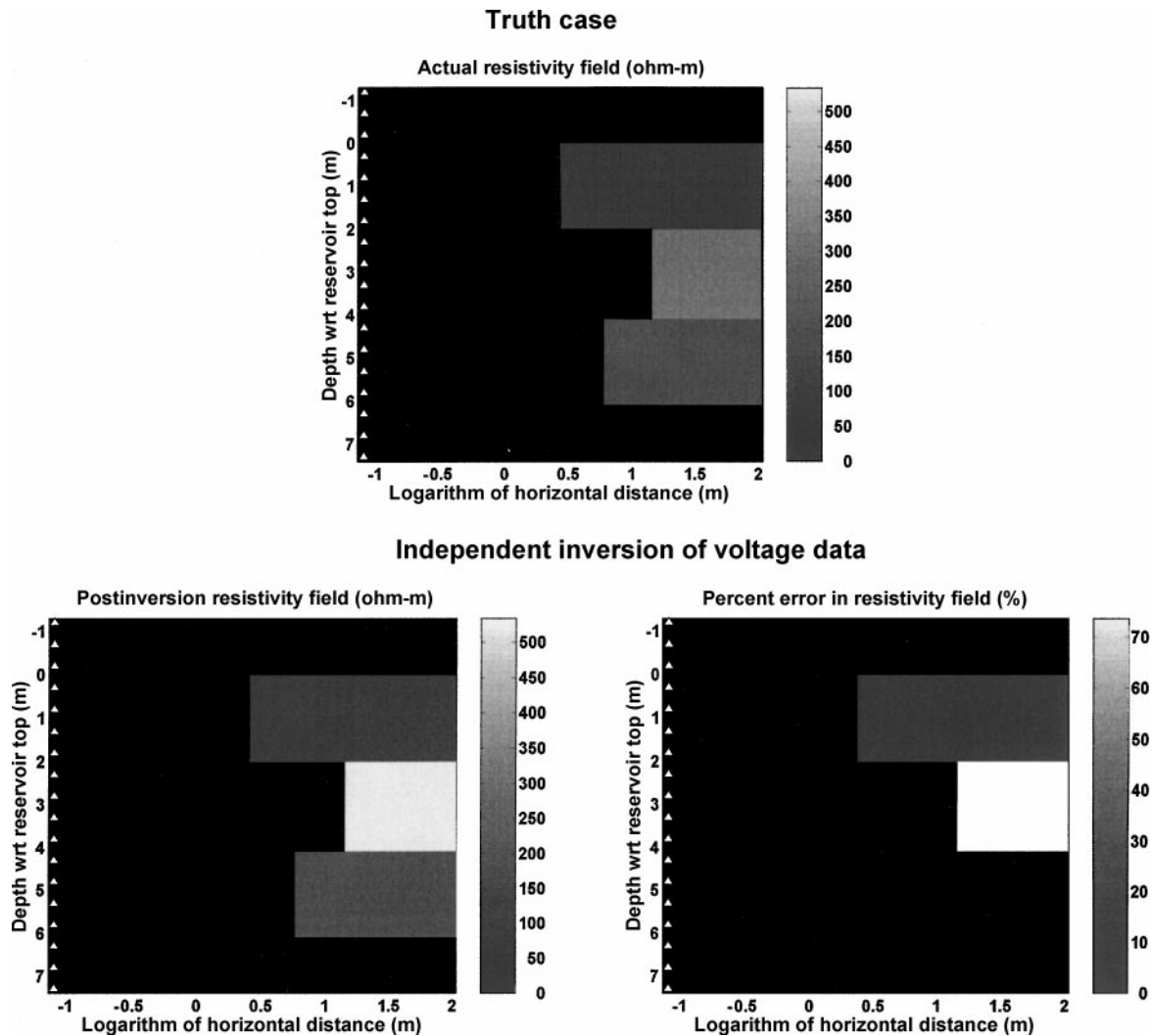### Percent error in permeability field (%)

Figure 8. Six-block formation example; comparisons of the inverted spatial distributions of permeability with the actual spatial distribution. Model-domain percent errors are also shown. The inverted spatial distributions of permeability were obtained using noisy single- and multipulse transient-pressure measurements, respectively. Transient pressure measurements are contaminated with 1% zero-mean Gaussian random noise. Locations of in-situ pressure sensors in the injection and observation wells are indicated with small circles. The term *wrt* = with respect to.

Although joint inversion of the noisy measurements captures the spatial distribution of permeability quite accurately, the permeability values for blocks located farther away from the injection well are slightly less accurate in comparison with the permeability values for blocks closer to the injection well. On the other hand, while resistivity values for the blocks neighboring the injection well remain accurate, inversion results for resistivity values divert significantly from the actual values for blocks located away from the injection well. These observations are consistent with the spatial resolution properties of in-situ transient pressure and dc resistivity measurements. Measurements acquired with the in-situ dc resistivity sensors exhibit high sensitivity to the resistivities in the vicinity of the injection well. In contrast to dc resistivity measurements, in-situ transient pressure measurements inherently exhibit a larger depth of penetration. Deployment of in-situ pressure sensors in the observation well helps to further constrain the spatial distribution of permeabilities. Therefore, permeability values

for blocks located far away from the injection well are more accurately reconstructed than the values of resistivity for the same blocks.

Despite the limitations of the joint inversion approach, numerical examples performed on noisy measurements clearly and conclusively indicate that the joint inversion approach yields more accurate reconstructions of the spatial distributions of both permeability and resistivity when compared to the results yielded by the independent inversion approach. On the other hand, for the cases of noise-free measurements, the impact of the joint inversion approach on the reconstruction of the spatial distributions of permeability and resistivity is negligible.

For inversions performed with noisy measurements, stability was achieved by setting the matrix $\mathbf{W}_m \cdot \mathbf{W}_{mi}^T$, equal to a unity diagonal matrix in equation 1. The Lagrange multiplier λ in equation 1 then takes the role of a Wiener regularization constant (Treitel and Lines, 1982). We implemented an

Figure 9. Six-block formation example; comparison of the inverted spatial distribution of resistivity with the actual spatial distribution. Model-domain percent errors are also shown. The inverted spatial distribution of resistivity was obtained using noisy dc resistivity measurements contaminated with 1% zero-mean Gaussian random noise. Locations of in-situ contact electrodes (resistivity sensors) in the injection well are indicated with small triangles. The term *wrt* = with respect to.

Truth case

Joint inversion of noise-free multipulse in-situ transient pressure and dc resistivity measurements (voltages)

Joint inversion of noisy multipulse in-situ transient pressure and dc resistivity measurements (voltages)
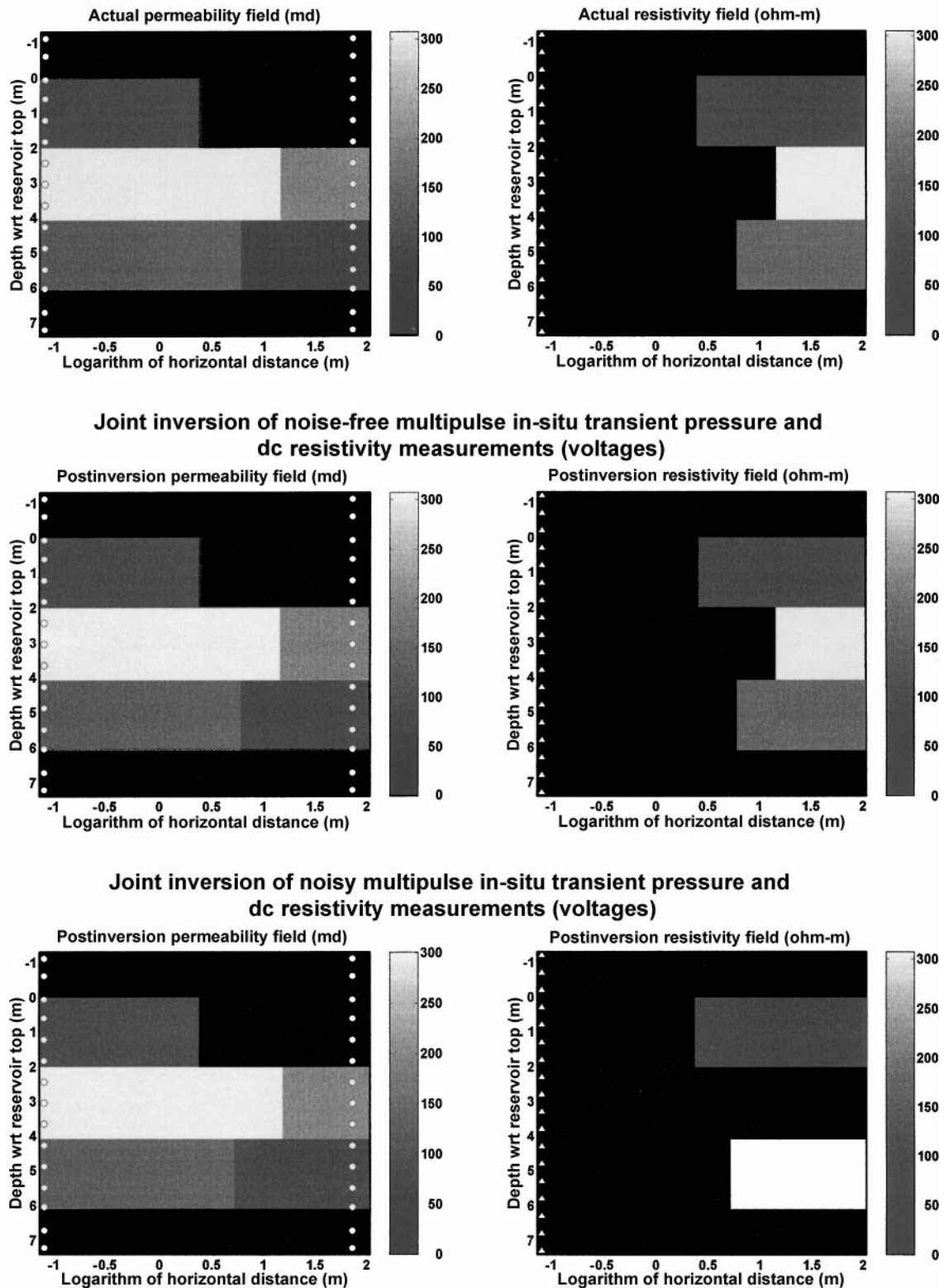

Figure 10. Six-block formation example; comparisons of the inverted spatial distributions of permeability and resistivity with the actual spatial distributions. The inverted spatial distributions of permeability and resistivity were obtained using both noise-free and noisy multipulse transient pressure and dc resistivity measurements, respectively. For the case of noisy data, 2% zero-mean Gaussian random noise was added to both transient pressure and dc voltage measurements. Locations of in-situ pressure sensors in the injection and observation wells are indicated with small circles, and locations of in-situ contact electrodes (resistivity sensors) in the injection well are indicated with small triangles. The term *wrt* = with respect to.

adaptive Lagrange multiplier search technique such that at the initial steps of the iteration, a relative misfit reduction of at least 75% was enforced at each iteration with respect to the data misfit achieved at the previous iteration (Torres-Verdín and Habashy, 1994). This approach assigns large λ values to equation 5 when $\Delta(\mathbf{m}^k) = \mathbf{m}^{k+l} - \mathbf{m}^k$ undergoes large variations in the initial steps of the iteration process. On the other hand, when $\Delta(\mathbf{m}^k)$ undergoes small variations, λ takes small values, hence allocating more weight to the first term of the cost function.

Application of dual-grid technique with joint inversion approach

When developing a methodology for joint inversion, we attempted to take full advantage of the large amount of information supplied by multiple types of permanent sensors. Use of large data sets, however, causes the inversion algorithm to lose the efficiency necessary to perform real-time estimation of petrophysical properties. One way to overcome this problem is to use unconventional yet fast and robust inversion schemes. To that end, we implemented a dual-grid inversion approach based on the cascade minimization technique introduced by Torres-Verdín et al. (2000). The algorithm consists of an inner loop in which the Jacobian matrix is approximated with finite-difference simulations performed on a coarse grid while an outer loop controls the global convergence through updates of data misfit computed with a fine finite-difference grid. Inner and outer loops can be designed in a flexible manner to improve convergence and to substantially reduce computation times. The computational performance of coarse-grid inner loop calculations can be further improved with the use of Broyden's rank-one update formula for the Jacobian matrix. Torres-Verdín et al. (2000) present the necessary convergence condition to be satisfied by the dual-grid inversion procedure.

Table 2 shows a comparison of computing times (clocked on a 300-MHz SGI Octane machine) required to perform the inversions of the six-block test case using various minimization strategies. The formation model considered for this inversion exercise is a slightly larger version of the six-block example described in the previous section. The computing times shown in Table 2 indicate that simple modifications to the inversion algorithm can produce sizable increments in computer efficiency, thereby making it feasible to invert large measurement sets into large spatial distributions of reservoir petrophysical properties.

Multiblock test case

A relatively more complex test case was designed to further assess the spatial resolution properties of arrays of in-situ permanent sensors of pressu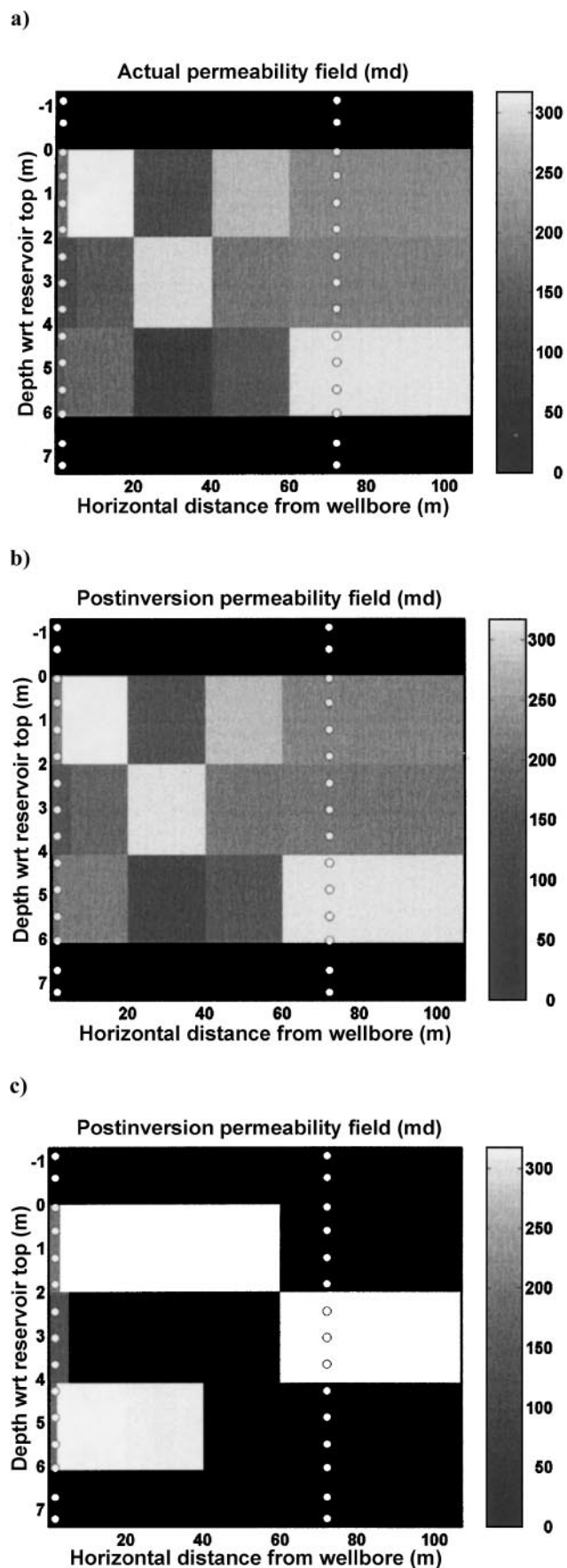re and dc electrical voltage. This test case consisted of 15 permeability block segments and 6 resistivity block segments. Again, the spatial distributions of permeability and resistivity are linked via block-boundary (water front) locations of the first and second radial petrophysical blocks for each horizontal layer. The remaining blocks in the permeability model reflect the spatial heterogeneity of intrinsic fluid absolute permeability. Therefore, in this case instead of a layer-by-layer uniform spatial distribution of permeability ahead of the water front, we investigate the inversion of laterally varying spatial distributions of permeability for each horizontal layer ahead of the front. The block-boundary locations other than the first one are not constrained by the resistivity data anymore; therefore, within the course of the inversion they are not allowed to vary. The locations of these block boundaries are assumed to be known from other types of measurements, i.e., seismic data acquired prior to the waterflood operation. Transient pressure and resistivity measurements exhibit joint sensitivity only to the location of the first block boundary that describes the location of the front within each horizontal layer. Therefore, the location of the first block boundary for each horizontal layer is pursued by the inversion along with the values of permeability and resistivity within each petrophysical block.

While generating the synthetic reservoir, we first assumed the permeability model and consistently linked the spatial distribution of porosity to the spatial distribution of permeability via the correlation given by $\phi(\mathbf{r}) = 0.1(\log_{10}[k(\mathbf{r})]) + 0.05$, which holds for shaly sandstone formations (Dussan et al., 1994). For the purpose of inversion, the spatial distribution of porosity is assumed to be known from other types of ancillary information such as seismic and well-log data. We considered the same well and sensor deployment described in the previous case. Transient pressure measurements were simulated assuming the same multiple flow-rate pulse schedule used in the six-block test case. Multipulse pressure measurements recorded between the 100th and the 300th hour of the flow-rate pulse schedule were input to the inversion. The inversion also included dc electrical voltages acquired at a single snapshot corresponding to the end of the transient pressure record. In addition to the inversions of noise-free measurements, we alternatively considered the case where both the simulated multipulse in-situ transient pressure and voltage measurements were contaminated with 2% zero-mean random Gaussian noise. For the noisy case, we used the same regularization strategy as for the inversions of noisy data in the six-block formation case.

Figures 11 and 12 describe results from joint inversions performed with both noise-free and noisy measurements. The actual spatial distributions of permeability and resistivity are shown in Figures 11a and 12a, respectively. Figure 11b displays noise-free joint inversion results for the spatial distribution of permeability, and Figure 12b shows joint inversion results for the spatial distribution of resistivity. Spatial distributions of permeability and resistivity obtained with the joint inversion

Table 2. Comparison of CPU execution times for the use of conventional and dual-grid inversion techniques.

Grid I size (outer loop), Jacobian computed via Fréchet derivatives	Grid II size (inner loop), Jacobian computed using Broyden's rank-one update formula	CPU time, (s)
$r \times z$ (EKSM) $- r$ (NKARD)	$r \times z$ (EKSM) $- r$ (NKARD)	
$105 \times 304 - 105$ nodes	Broyden update formula not utilized	8566.7
$105 \times 304 - 105$ nodes	$105 \times 304 - 105$ nodes	6448.9
$105 \times 304 - 105$ nodes	$54 \times 204 - 54$ nodes	4486.8

a)

Actual permeability field (md)

b)

Postinversion permeability field (md)

c)

Postinversion permeability field (md)

of noisy measurements are displayed in Figures 11c and 12c, respectively. In the frames of Figures 11 and 12, the spatial dimensions encompassed by the horizontal axes differ by orders of magnitude, i.e., 2 m versus 100 m, respectively. Inversion results obtained from noise-free measurements indicate an accurate reconstruction of the spatial distributions of permeability and resistivity. No regularization was required for this case. Transient pressure measurements acquired in both the injection and observation wells appear to have sufficient sensitivity to resolve the radially heterogeneous distribution of permeability. Resistivity measurements in the injection well, on the other hand, help to accurately constrain the location of the oil–water interface.

For the case of joint inversion of noisy measurements, permeability and resistivity values for blocks closest to the injection well are estimated more accurately than for blocks located farther from the injection well. The same regularization approach used for the inversion of noisy measurements in the case of a six-block formation is used in this case. Estimated block-boundary (fluid front) locations for the first and second radial petrophysical blocks remain consistent with the actual locations. Yet reconstructions of both permeability and resistivity values beyond the block-boundary locations depart significantly from the original values. Inversion results obtained with noisy measurements are indicative of the resolution properties inherent to both types of measurements. Voltages measured by this array lack the length penetration necessary to resolve resistivity values far away from the injection well.

In contrast to dc resistivity measurements, in-situ transient pressure measurements exhibit a longer depth of penetration. However, their lateral resolution is not sufficient to resolve the spatial details of the original permeability model. Farther away from the injection well, only an average value for permeability can be reconstructed for each layer. In this case, deployment of in-situ pressure sensors in the observation well did not help to further constrain the spatial distribution of permeabilities. The lateral resolution of in-situ transient pressure measurements acquired in the observation well is limited because of the equilibration of in-situ transient pressure responses away from the injection well. This equilibration results from hydraulic communication among petrophysical blocks. As a result, in-situ transient pressure measurements acquired in the observation well can only resolve a relatively simple distribution of volumetric average permeabilities for each layer. More spatially complex variations of permeability and resistivity can be reconstructed with the joint inversion of in-situ transient pressure and dc resistivity measurements for significantly low noise levels.

Figure 11. Multiblock formation example, with comparisons of inverted and actual spatial distributions of permeability. (a) Actual spatial distribution of permeability. The inverted spatial distribution of permeability was obtained using (b) noise-free and (c) noisy multipulse transient pressure and dc resistivity measurements, respectively. For the inversions with noisy data, 2% zero-mean Gaussian random noise was added to both transient pressure and dc voltage measurements. Locations of in-situ pressure sensors in the injection and observation wells are indicated with small circles. The term *wrt* = with respect to.

Discussion on the inversion results

Undoubtedly, permeable rock formations to be encountered in practical applications will be more spatially and petrophysically complex than the idealized synthetic models assumed in this paper. Despite the spatial complexity of the underlying petrophysical model, the inversion results described in our numerical experiments indicate that the joint use of in-situ transient pressure and resistivity measurements improves the accuracy of the quantitative estimation of resistivity and permeability. Comparisons of the inversion results obtained from independent and joint inversions of noisy measurements (for the six-block formation case) clearly indicate that the concomitant use of transient pressure and resistivity measurements reduces nonuniqueness in the estimated model. On the other hand, the inversion tools developed in this paper could also be used to design the deployment of sensors to optimally detect and quantify reservoir properties constrained by specific geometrical and petrophysical conditions.

Having established a quantitative proof of concept for the joint inversion of resistivity and transient pressure measurements, we remark that the assumptions placed on the fluid-flow model can be further relaxed by using a multiphase flow formulation for modeling transient pressure responses as well as spatial distributions of fluid saturation. Furthermore, the salinity contrast between the injected and in-situ fluids can be taken into account by solving a transport equation, namely, a convection-diffusion equation in addition to multiphase flow equations. Using a multiphase, multicomponent flow simulator, we can iteratively model spatial distributions of fluid saturations and salt concentrations in addition to other fluid-flow measurements such as pressure and fractional rates of flowing phases. Therefore, spatial distributions of fluid saturations and salt concentrations can be simulated in response to perturbations to spatial distributions of petrophysical parameters—for example, absolute fluid permeability and formation porosity within a joint inversion framework. Subsequently, spatial distributions of fluid saturations and salt concentrations can be used for computing spatial distributions of resistivity using appropriate saturation and salt concentration equations. As such, perturbations to petrophysical parameters, i.e., permeability and porosity, can be propagated to the resistivity domain. An electromagnetic (or dc resistivity) simulator can be used to simulate resistivity measurements in response to the perturbed resistivity model. In conclusion, quantitative estimations of spatial distributions of permeability and porosity can
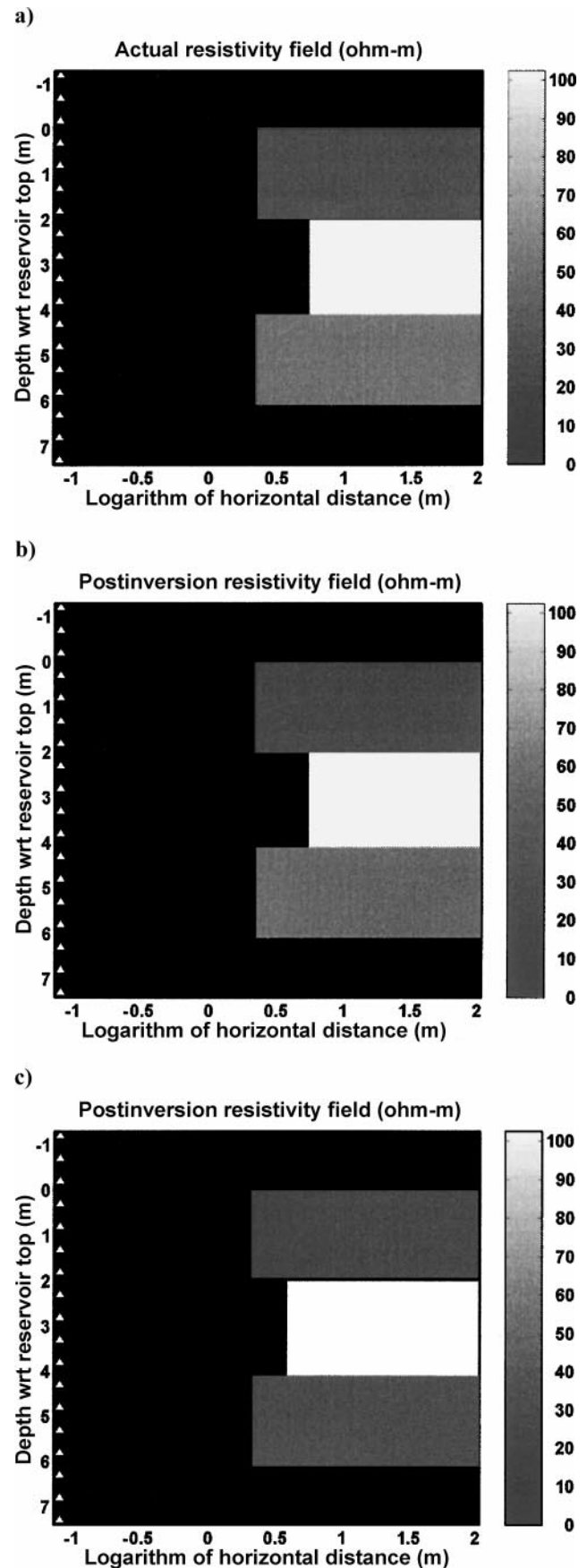
Figure 12. Multiblock formation example, with comparisons of inverted and actual spatial distributions of resistivity. (a) Actual spatial distribution of resistivity. The inverted spatial distribution of resistivity was obtained using (b) noise-free and (c) noisy multipulse in-situ transient pressure and dc resistivity measurements, respectively. For the inversions with noisy data, 2% zero-mean Gaussian random noise was added to both transient pressure and dc voltage measurements. Locations of in-situ contact electrodes in the injection well are indicated with small triangles. Note that in the frames of this figure, the horizontal distance is presented on a logarithmic scale unlike the case of plots that show the spatial distribution of permeability for the multiblock formation example. The term *wrt* = with respect to.

be performed honoring both fluid-flow and resistivity domain measurements.

One possible limitation of the described algorithm is the computational cost of multiphase fluid-flow simulations within an iterative inversion algorithm that requires the computation of the Jacobian matrix. However, for an inversion problem that can be described using a reasonable number of parameters and that requires a relatively short time scale of multiphase flow, the described joint inversion approach remains practical. A successful application of the multiphase joint inversion algorithm is described by Alpak, Habashy, et al. (2003) for the simultaneous estimation of layer-by-layer permeability and porosities from electromagnetic induction logging and wireline formation tester transient pressure measurements.

CONCLUSIONS

Our inversion results constitute a proof-of-concept exercise to appraise the spatial resolution properties of transient pressure and dc resistivity measurements acquired with in-situ permanent sensors. For all of the cases investigated, the joint inversion of in-situ transient pressure and dc resistivity measurements improved the accuracy of estimations compared to separately inverting either data type. This was possible because simultaneous use of the two measurement sets naturally reduced nonuniqueness and hence improved stability. However, coupling of the two measurement sets is nontrivial. Ideally, a rigorous multiphase fluid-flow formulation should be used to drive the simulation and inversion of the two measurement sets. The inversion exercises presented in this paper were based on an approximate formulation of multiphase flow that allowed us to couple pressure diffusion and electrical phenomena through geometrical parameters. The future challenge is to couple the two phenomena in more complicated cases of fluid saturation transitions and salt mixing between injected and connate formation water.

Technical issues explored in this paper included (1) noisy and imperfect data sampling strategies and (2) modalities for the flow rate excitation of in-situ transient pressure measurements. A multitude of sensor and measurement configurations could be further explored to appraise the relative influence of these issues on the accuracy and stability of the inversions. The inversion examples suggest that the cooperative use of in-situ transient pressure and in-situ dc resistivity measurements does provide an efficient way to detect and quantify petrophysical changes due to fluid-flow dynamics in the vicinity of the sensors. However, because of the underlying diffusion phenomena governing the two sets of measurements, the spatial resolution of the inversion deteriorates with distance away from sources and detectors. It is envisioned that the deployment of arrays of in-situ permanent sensors should be designed to selectively adjust the sensitivity and resolution to shallow and deep spatial regions in the reservoir.

ACKNOWLEDGMENTS

REFERENCES

Alpak, F. O., T. M. Habashy, C. Torres-Verdín, and V. E. B. Dussan, 2003, Joint inversion of pressure and time-lapse electromagnetic logging measurements: 44th Annual Symposium, Society of Professional Well Log Analysts, SS1–SS14.

Alpak, F. O., C. Torres-Verdín, and K. Sepehrnoori, 2001, Numerical simulation and inversion of pressure data acquired with permanent sensors: Annual Technical Conference and Exhibition, Society of Petroleum Engineers, paper SPE 71612.

Alpak, F. O., C. Torres-Verdín, K. Sepehrnoori, S. Fang, and L. Knizhnerman, 2003, An extended Krylov subspace method to simulate single-phase fluid flow phenomena in axisymmetric and anisotropic porous media: Journal of Petroleum Science and Engineering, **40**, No. 3, 121–144.

Archie, G. E., 1942, The electrical resistivity log as an aid in determining some reservoir characteristics: Petroleum Transactions, AIME, **146**, 54–62.

Athichanagorn, S., R. N. Horne, and J. Kikani, 1999, Processing and interpretation of long term data from permanent downhole pressure gauges: Annual Technical Conference and Exhibition, Society of Petroleum Engineers, paper SPE 56419.

Babour, K., A. K. Belani, and J. Pilla, 1995, Method and apparatus for long term monitoring of reservoirs: United States Patent 5 467 823.

Babour, K., A. K. Belani, and B. Seeman, 1997, Method and apparatus for surveying and monitoring a reservoir penetrated by a well including fixing electrodes hydraulically isolated with a well: United States Patent 5 462 051.

Baker, A., J. Gaskell, J. Jeffery, A. Thomas, T. Veneruso, and T. Unneland, 1995, Permanent monitoring—Looking at lifetime reservoir dynamics: Oilfield Review, **7**, No. 4, 32–46.

Belani, A., T. S. Ramakrishnan, T. M. Habashy, F. Kuchuk, and L. Ayesteran, 2000, Method and apparatus for characterizing earth formation properties through joint pressure-resistivity inversion: United States Patent 6 061 634.

Bryant, I. D., M.-Y. Chen, B. Raghuraman, I. Raw, J.-P. Delhomme, C. Chouzenoux, D. Pohl, Y. Manin, E. Rioufol, G. Oddie, D. Swager, and J. Smith, 2002a, An application of cemented resistivity arrays to monitor waterflooding of the Mansfield sandstone, Indiana, USA: SPE Reservoir Evaluation and Engineering, **5**, No. 6, 447–454.

Bryant, I. D., M.-Y. Chen, B. Raghuraman, R. Schroeder, M. Supp, J. Navarro, I. Raw, J. Smith, and M. Scaggs, 2002b, Real-time monitoring and control of water influx to a horizontal well using advanced completion equipped with permanent sensors: Annual Technical Conference and Exhibition, Society of Petroleum Engineers, paper SPE 77522.

Buckley, S. E., and M. C. Leverett, 1942, Mechanism of fluid displacement in sands: Petroleum Transactions, AIME, 146, 107–116.

Charara, M., Y. Manin, C. Bacquet, and J.-P. Delhomme, 2002, Use of permanent resistivity and transient-pressure measurement for time-lapse saturation mapping: SPE Reservoir Evaluation and Engineering, **5**, No. 6, 472–479.

Druskin, V., and L. A. Knizhnerman, 1987, A method of solution of forward problems of electric well logging and electric exploration with direct current (Russian, translated into English): Izvestiya, Earth Physics, **23**, 317–323.

Dussan, V. E. B., B. I. Anderson, and F. Auzerais, 1994, Estimating vertical permeability from resistivity logs: 35th Annual Logging Symposium, Society of Professional Well Log Analysts, 441–4425.

Ellis, R. G., C. G. Farquharson, and D. W. Oldenburg, 1993, Approximate inverse mapping inversion of the COPROD2 data: Journal of Geomagnetism and Geoelectricity, **45**, 1001–1012.

Gill, P. E., W. Murray, and M. H. Wright, 1981, Practical optimization: Academic Press Inc.

Muskat, M., 1937, The flow of homogeneous fluids through porous media: McGraw-Hill Book Company.

Raghuraman, B., and T. S. Ramakrishnan, 2001, Interference analysis of cemented-permanent-sensor data from a field experiment: Conference, European Association of Geoscientists and Engineers Extended Abstracts, MO19.

Ramakrishnan, T. S., and F. J. Kuchuk, 1993, Pressure transients during injection: Constant rate and convolution solutions: Transport in Porous Media, **10**, 103–136.

Torres-Verdín, C., and T. M. Habashy, 1994, Rapid 2.5-D forward modeling and inversion via new nonlinear scattering approximation: Radio Science, **29**, 1051–1079.

Torres-Verdín, C., V. Druskin, S. Fang, L. Knizhnerman, and A. Malinverno, 2000, A dual-grid nonlinear inversion technique with applications to the interpretation of dc resistivity data: Geophysics, **65**, 1733–1745.

Treitel, S., and L. R. Lines, 1982, Linear inverse theory and deconvolution: Geophysics, **47**, 1153–1159.

van Kleef, R., R. Hakvoort, V. Bushan, S. Al-Khodhori, W. Boom, C. de Bruin, K. Babour, C. Chouzenoux, J.-P. Delhomme, Y. Manin, D. Pohl, E. Rioufol, M. Charara, and R. Harb, 2001, Water flood monitoring in an Oman carbonate reservoir using a downhole permanent electrode array: Middle East Oil Show, Society of Petroleum Engineers, paper SPE 68078.

Wang, P., and R. N. Horne, 2000, Integrating resistivity data with production data for improved reservoir modeling: Asia Pacific Conference on Integrated Modelling for Asset Management, Society of Petroleum Engineers, paper SPE 59425.